Theoretical Study of Dual-Core Photonic Crystal Fibers With Metal Wire

Shuyan Zhang, Member, IEEE
Xia Yu, Senior Member, IEEE
Ying Zhang
Ping Shum, Senior Member, IEEE
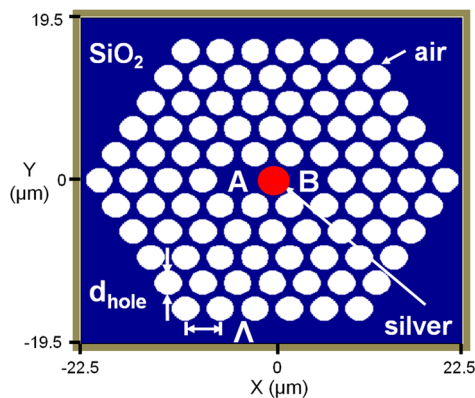Yating Zhang, Member, IEEE
Li Xia
Deming Liu

Theoretical Study of Dual-Core Photonic Crystal Fibers With Metal Wire

Shuyan Zhang,[1] *Member, IEEE*, **Xia Yu,**[1] *Senior Member, IEEE*, **Ying Zhang,**[1]
Ping Shum,[2] *Senior Member, IEEE*, **Yating Zhang,**[1,3] *Member, IEEE*,
Li Xia,[3] **and Deming Liu**[3]

[1]Singapore Institute of Manufacturing Technology, Singapore 638075
[2]School of EEE, Nanyang Technological University, Singapore 639798
[3]Wuhan National Laboratory for Optoelectronics, Wuhan 430074, China

Abstract: In this paper, we, for the first time, systematically study a new structure of a dual-core photonic crystal fiber filled with a metal wire in the center air hole. Theoretical analysis based on the supermode theory and the coupled-mode theory shows that the directional power transfer between the two fiber cores is enhanced by the resonant coupling between the surface plasmon modes and the fiber core-guided modes. A coupling length reduction of more than one order of magnitude is demonstrated for the new structure in the near-infrared regime. As a new fiber coupler device, the highest coupling efficiency is 81.82%, the insertion loss is as low as 0.87 dB, and the extinction ratio is 30.54 dB at 1550 nm for the optimized design configuration. The new structure is compact in size and easy to fabricate, making it promising for miniaturized complex communication devices.

Index Terms: Plasmonics, waveguides, fiber optics systems.

1. Introduction

The latest trend in the development of all-fiber devices is the high-level integration of fiber functionalities into a photonic device. Among all the functions, controllable directional power transfer between fiber cores is of particular interest and is referred to as the workhorse of fiber components [1]. Recently, several research groups have reported the use of dual-core photonic crystal fibers (DC-PCFs), where two adjacent solid cores are placed close to each other into a single PCF as optical fiber couplers because of their vast design possibilities, large index contrast, and compactness in size [2], [3]. However, the coupling length of the device is strongly dependent on the fiber structure and is generally long, which results in a low coupling efficiency (CE). This can cause problems in many communication applications such as intermodal dispersion in signal pulse transmission [4].

In this paper, we, for the first time, propose the use of a metal wire in the center of the DC-PCF to enhance the directional power transfer. Metal wires in fiber waveguides have attracted a lot of attention in recent years, which are mainly focused on the polarization characteristics and transmission characteristics, for example [5]–[7]. We show that the resonant coupling between the surface plasmon (SP) modes supported by the metal wire and the fiber core-guided modes can also be used to enhance the dual-core fiber coupler performance with a one-order-of-magnitude
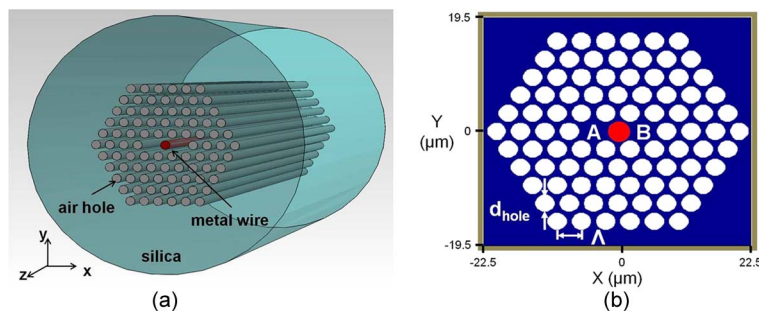
Fig. 1. (a) A new DC-PCF structure filled with a metal wire in the center (red). (b) The simulation model of the new structure. The gray area is the PML region (not drawn on scale).

reduction in coupling length and improvement on CE. At the same time, the filling of a metal wire keeps the compactness of the PCF structure and is easy to fabricate. These features will demonstrate advantages of our new structure in miniaturized complex communication devices such as photonic integrated devices [8], wavelength multiplexing systems [2], and optical switches [4].

We present our systematic study of the new structure in this paper, which is organized in the following way: Section 1 gives an overview of the paper and highlights its contribution. Section 2 describes the new structure. Section 3 explains in detail the theoretical modeling of the new structure by the supermode theory (SMT) and the coupled-mode theory (CMT). Section 4 discusses the modeling results of the new structure as a novel fiber coupler design in terms of various performance indicators. The effect of fiber microstructure parameter variation and different metal coating configurations is also discussed for performance optimization. Section 5 summarizes the key findings and points out its future impact.

2. New Structure

Fig. 1(a) is the new DC-PCF structure filled with a metal wire (silver) in the center shown as red. Many techniques are available to realize this structure, i.e., selective filling of a metal wire into a conventional dielectric DC-PCF, such as pressure-assisted pumping [9] or using femtosecond laser micromachining [10]. Fig. 1(b) is the simulation model, $d_{hole} = 2\ \mu$m, $\Lambda = 3.75\ \mu$m. The structural parameters were chosen based on our existing available DC-PCF. The two cores are named A and B for easy illustration. The dielectric property of silica is described by the Sellmeier equation [11] and silver by the Drude model [12]. The simulation was carried out using the *FemSIM* software to find the complex propagation constants of the waveguide modes with the finite-element method. To properly estimate the fiber confinement loss, a perfectly matching layer (PML) was also added.

3. Theoretical Modeling of DC-PCF With Metal Wire

For a systematic and complete study, we used two approaches for the analysis of power coupling in the new structure. SMT obtains the propagating hybrid modes of the multiwaveguide system as a whole, whereas CMT analyzes the multiwaveguide system by calculating the eigenmode of each individual waveguide under the perturbation of other waveguides. We analyzed the mode characteristics for the x-polarized direction, but the same principles can be applied to the y-polarized modes without losing generality.

3.1. SMT for DC-PCF With Metal Wire

In SMT, the power coupling is described by the interference of the fiber core-guided even and odd supermodes, denoted as e- and o-, respectively. Their electric field profiles are shown in Fig. 2. The even supermode is symmetric about the *y*-axis, whereas the odd supermode is symmetric about the origin. It is pointed out in [13] that higher order modes do not contribute to the intercore power
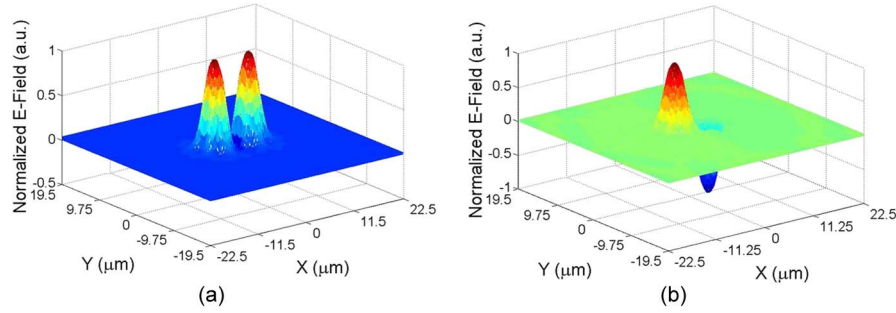
Fig. 2. Electric field profiles of (a) an even supermode and (b) an odd supermode of the new DC-PCF structure filled with a metal wire in the center.

transfer; hence, only the fundamental core-guided modes were discussed in this paper. The effective refractive indices (n_{eff}) of various modes were obtained, the real part $\text{Re}(n_{eff})$ is related to the propagation constant $\beta = 2\pi/\lambda \times \text{Re}(n_{eff})$ of the mode, and the imaginary part $\text{Im}(n_{eff})$ is related to the confinement loss $\alpha = (20/\ln 10) \times 2\pi/\lambda \times \text{Im}(n_{eff})$ (in dB per unit length). For the conventional unfilled dielectric DC-PCF, the total interference transverse electric field $\bar{E}(x, y, z)e^{-jwt}$ can be expressed by (1), where M is the amplitude, and ϕ is the phase shift; c is the relative excitation amplitude ranging from 0 to 1 based on the normalization condition $c_e^2 + c_o^2 = 1$. Since the power is proportional to $|\bar{E}|^2$, the power of the two cores P_A and P_B can be expressed as (2). Now, considering the metal-introduced absorption, the electric field amplitude needs to be replaced by $E'_e = E_e \times 10^{-(\alpha_e z/20)}$ and $E'_o = E_o \times 10^{-(\alpha_o z/20)}$. Given the fact that $E_e(-x, y) = E_e(x, y)$ and $E_o(-x, y) = -E_o(x, y)$, we can derive the transmission characteristics of a DC-PCF filled with a metal wire. The transmittance function $T'(z)$ is described as the proportion of power transferred to the other core from the launching core at a given position z along the fiber length as expressed by (3). For clarity and simplicity, we assumed $c_e = c_o$ and $E_e = E_o$. At $z = 0$, the total interference field showed a concentration of optical power at core B; hence, we could make an analogy the incident energy was launched in core B and subsequently transferred to core A

$$
\begin{cases}
\bar{E}(x, y, z)e^{-jwt} = \left[M(x, y, z)e^{j\phi(x,y,z)} \right] e^{j[(\beta_e + \beta_o)/2z - wt]} \\
M = \sqrt{c_e^2 E_e^2 + c_o^2 E_o^2 + 2c_e c_o E_e E_o \cos[(\beta_e - \beta_o)z]} \\
\phi = \tan^{-1}\left[\frac{c_e E_e - c_o E_o}{c_e E_e + c_o E_o} \times \tan\left(\frac{\beta_e - \beta_o}{2}z\right) \right]
\end{cases}
\tag{1}
$$

$$
\begin{cases}
P_A(z) = M^2(-x, y, z) = c_e^2 E_e^2(-x, y) + c_o^2 E_o^2(-x, y) + 2c_e c_o E_e(-x, y)E_o(-x, y)\cos[(\beta_e - \beta_o)z] \\
P_B(z) = M^2(x, y, z) = c_e^2 E_e^2(x, y) + c_o^2 E_o^2(x, y) + 2c_e c_o E_e(x, y)E_o(x, y)\cos[(\beta_e - \beta_o)z]
\end{cases}
\tag{2}
$$

$$
\begin{cases}
T'(z) = \frac{P'_A(z)}{P'_B(0)} = \left[\frac{\psi(z)}{2} \right]^2 + \varphi(z) \times \sin^2\left(\frac{\beta_e - \beta_o}{2}z\right) \\
\psi(z) = 10^{-(\alpha_e z/20)} - 10^{-(\alpha_o z/20)} \\
\varphi(z) = 10^{-[(\alpha_e + \alpha_o)z/20]}.
\end{cases}
\tag{3}
$$

Fig. 3(a) shows the wavelength-dependent $\text{Re}(n_{eff})$ of different modes in the fiber. The red and blue curves represent the dispersion of the fiber core-guided modes in a DC-PCF without and with a metal wire, respectively. The solid curves are for the even supermodes, and the dashed curves are for the odd supermodes. The black dotted curves represent different orders of SP modes excited on an isolated metal wire surrounded by the air hole lattice embedded in the silica background. The insets show their longitudinal Poynting vector distribution. First, it can be seen that the fundamental and first-order SP modes (SP^0 and SP^1) have much higher effective refractive indices, and hence, their dispersion curves do not intersect with those of the fiber core-guided modes. Second, the difference $|\text{Re}(n_{eff}^e) - \text{Re}(n_{eff}^o)|$ is much larger for the blue solid and dashed curves compared with
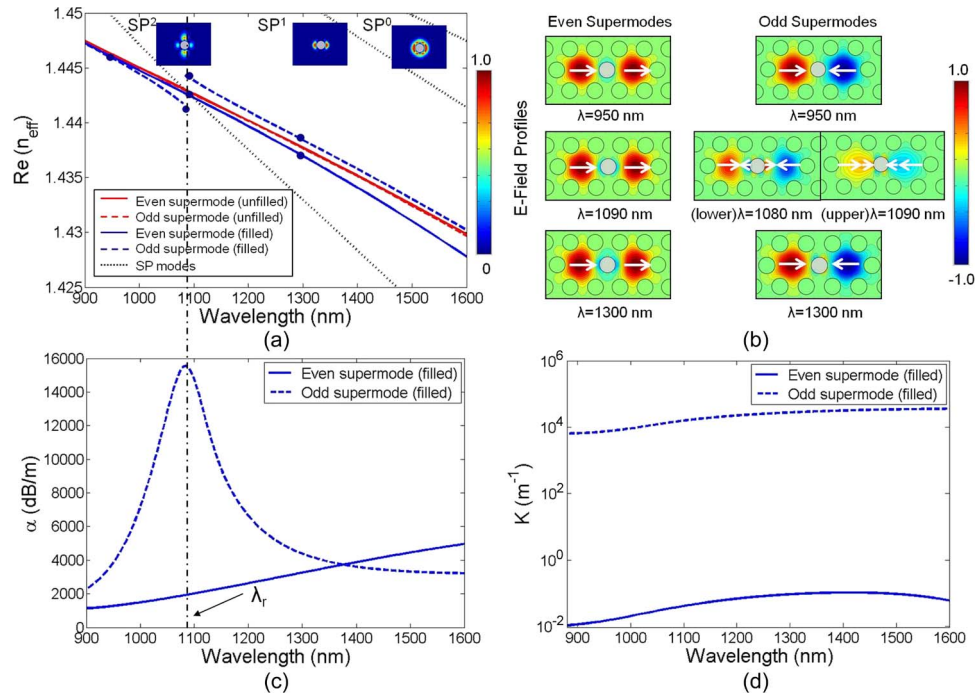
Fig. 3. (a) Wavelength dependence of the real part of the effective refractive indices of the supermodes and SP modes. The insets show the magnitude of the longitudinal Poynting vector of the SP modes. (b) Electric field profiles of the even and odd supermodes of the new structure at specific wavelengths indicated by the blue dots in (a). The white arrows are the electric field directions. (c) Loss spectrum of the even and odd supermodes of the new structure. The black dash-dotted vertical line shows the resonant wavelength position λ_r. (d) Coupling strength comparison of the even and odd supermode coupling with the SP^2 mode.

that of the almost overlapped two red curves in the whole wavelength range investigated. The reason for this large difference in value is that resonant coupling occurs between the second-order SP mode (SP^2) and the core-guided odd supermode whose parities are matched. At the resonant coupling wavelength $\lambda_r = 1090$ nm, these two modes are phase matched. Their dispersion curves (the SP^2 black dotted curve and the red dashed curve) intersect at this wavelength, resulting in an anticrossing of the blue dashed curve. However, no significant coupling occurs between the SP^2 mode and the core-guided even supermode, so the blue solid curve is continuous and decreases gradually with the wavelength.

The various mode profiles at specific wavelengths indicated in Fig. 3(a) (the blue dots) are plotted in Fig. 3(b). They represent the mode profiles before, at, and after the resonant coupling. The white arrows indicate the electric field directions. We discuss the SP^2 mode and the odd supermode coupling first. At $\lambda = 950$ nm before the resonant coupling, the electric field is confined within core areas. At $\lambda = \lambda_r = 1090$ nm, the coupling between the SP^2 mode and the core-guided odd supermode is the strongest. Therefore, two odd hybrid supermodes are formed with the left one (the lower branch) describing the opposite phase coupling, i.e., with different field directions, and the right one (the upper branch) describing the coordinate phase coupling, i.e., with the same field direction. The lower branch of the blue dashed curve describes the fundamental mode transition from the fiber core mode like to the SP mode like as λ increases, whereas the upper branch describes the opposite process. At $\lambda = 1300$ nm after the resonant coupling, most of the electric field couples back to the fiber cores. As for the core-guided even supermodes, the electric field is confined within the core areas throughout the wavelength range. There is no resonant coupling between the SP^2 mode and the even supermode because their field parities do not match; their field overlap integral value is small.

To further elaborate the difference between the even and odd supermodes in the new structure, the loss spectrum (α) is plotted in Fig. 3(c), and the coupling strength (κ) is plotted in Fig. 3(d). First, the peak in the loss spectrum of a core-guided mode is often used to identify λ_r because at this wavelength, maximum power is transferred from the fiber cores to the metal wire [6]. Thus, in our new structure, only the odd supermode exhibits a peak loss value as can been seen from the blue dashed curve. The λ_r identified in this way agrees well with the anticrossing wavelength in Fig. 3(a) marked by the black dash-dotted vertical line. Moreover, at λ_r, the loss of the odd supermode is much larger than that of the even supermode. Second, the field overlap integral of the SP^2 mode and the core-guided supermodes was quantified by the κ value, similar to [14], the larger the κ value, the stronger the coupling. It is evident in Fig. 3(d) that κ^{odd} is 10^6 times larger than κ^{even}, which confirms that resonant coupling can only happen between the SP^2 mode and the fiber core-guided odd supermode.

3.2. CMT for DC-PCF With Metal Wire

In CMT, the characteristics of the modes of a multiwaveguide system are determined by a set of coupling equations. The rigorous derivation of CMT considering the cross power term and self-coupling term is shown in (4), where $A(z)$ and $B(z)$ express the z-dependence of the individual guided modes; $\delta = (\beta_2 - \beta_1)/2$ is the average difference between their propagation constants [15]. Other parameters are defined in (5), where γ_{pq} ($p, q = 1, 2$ referring to the individual waveguide I and II, respectively) is the mode coupling coefficient of the system, c_{pq} is the butt coupling coefficient between the two individual waveguides, and χ_p can be understood as the self-coupling coefficient shown in (6). N_p is a normalization factor describing the time average propagation power of each individual waveguide. The underlying assumption for these equations to be valid is that the modal fields after mode coupling do not differ substantially from those before coupling, which is equivalent to $|\kappa_{pq}| \ll |\beta_p|, |\beta_q|$ for a weak coupling condition [16]

$$\begin{cases} \frac{dA}{dz} = -j\gamma_a B\exp(-j2\delta z) + j\sigma_a A \\ \frac{dB}{dz} = -j\gamma_b A\exp(j2\delta z) + j\sigma_b B \end{cases} \tag{4}$$

$$\begin{cases} \gamma_a = (\gamma_{12} - c_{12}\chi_2)/(1 - c_{12}c_{21}) \\ \gamma_b = (\lambda_{21} - c_{21}\chi_1)/(1 - c_{12}c_{21}) \\ \sigma_a = (\gamma_{21}c_{12} - \chi_1)/(1 - c_{12}c_{21}) \\ \sigma_b = (\gamma_{12}c_{21} - \chi_2)/(1 - c_{12}c_{21}) \end{cases} \tag{5}$$

$$\begin{cases} \gamma_{pq} = \frac{\pi}{2\lambda}\sqrt{\frac{\varepsilon_0}{\mu_0}}\frac{\int_{-\infty}^{\infty}\int_{-\infty}^{\infty}(n^2-n_q^2)E_p^* \bullet E_q dxdy}{N_p} \\ c_{pq} = \frac{\int_{-\infty}^{\infty}\int_{-\infty}^{\infty}u_z\bullet(E_p^*\times H_q + E_q\times H_p^*)dxdy}{4N_p} \\ \chi_p = \frac{\pi}{2\lambda}\sqrt{\frac{\varepsilon_0}{\mu_0}}\frac{\int_{-\infty}^{\infty}\int_{-\infty}^{\infty}(n^2-n_p^2)E_p^* \bullet E_p dxdy}{N_p} \\ N_p = \frac{1}{2}\int_{-\infty}^{\infty}\int_{-\infty}^{\infty}\left(E_p\times H_p^*\right)\bullet u_z dxdy. \end{cases} \tag{6}$$

In our structure, the weak coupling condition was satisfied by taking the individual waveguide I as shown in Fig. 4(a) and treating the right core in Fig. 4(b) as perturbation, similarly for waveguide II. Their electric and magnetic field distribution of mode ($E_{p,q}$ and $H_{p,q}$) were calculated using *FemSIM* simulation. The power coupling characteristics are described by (7)–(9). $\beta_{\pm}$ are the propagation constants of the modes in the multiwaveguide system similar to the β in SMT, which were computed from (7). The power inside core A and core B was obtained from (8) by solving $A(z)$ and $B(z)$ assuming the initial launching power is in one core only, say core B, i.e., $A(0) = 0$ and $B(0) = 1$, to be consistent with the SMT condition. It is evident that the power coupling in between the two cores
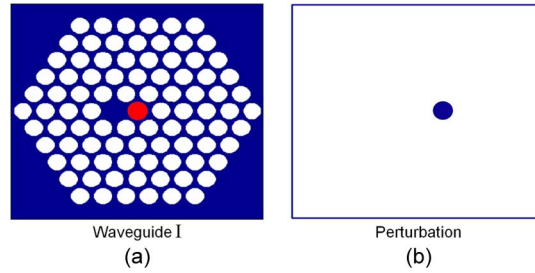
Fig. 4. (a) The structure of individual waveguide I and (b) the right core as a refractive index perturbation to waveguide I.
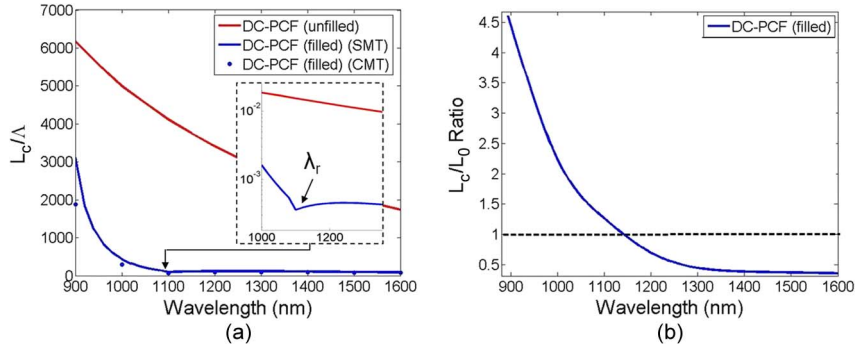

Fig. 5. (a) Results of the coupling length of a DC-PCF with and without a metal wire calculated from SMT and CMT. The inset is a zoom-in view showing the coupling length reduction in a log scale. (b) L_c/L_0 ratio versus wavelength for the DC-PCF filled with a metal wire. The black dashed line marks the threshold value.

is periodic, and the maximum power transfer occurs at every z position defined in (9). These computation results are compared with the SMT results in Section 4

$$\begin{cases} \beta_\pm = \left(\frac{\beta_1+\beta_2}{2} - \frac{\sigma_a+\sigma_b}{2}\right) \pm Q \\ Q = \sqrt{\left(\delta + \frac{\sigma_a-\sigma_b}{2}\right)^2 + \gamma_a\gamma_b} \end{cases} \tag{7}$$

$$\begin{cases} P_A(z) = A \bullet A^* = \frac{\gamma_a^2}{Q^2}\sin^2(Qz) \\ P_B(z) = B \bullet B^* = 1 - \frac{\gamma_a\gamma_b}{Q^2}\sin^2(Qz) \end{cases} \tag{8}$$

$$z = \frac{\pi}{2Q}(2m+1) \quad (m = 0, 1, 2, \ldots). \tag{9}$$

4. Modeling Results and Discussions of the New Fiber Coupler

4.1. Coupler Characteristics

From the SMT point of view, for constructive interference, the peak power occurs in one core, and if destructive interference occurs, power transfers to the other core. This power transfer is periodic in nature as can been seen from (3). The coupling length (L_c) is defined as the shortest fiber length, where the maximum power transfer occurs between the two cores and is considered as a key parameter to characterize a coupler. L_c is expressed in (10). From the equation, L_c is inversely proportional to the difference between the Re(n_{eff}) value of the even and the odd supermode. The normalized L_c value with respect to the pitch size Λ is shown in Fig. 5(a) as a variation with the wavelength. As discussed in Section 3.1 Fig. 3(a), the resonant coupling in the new structure
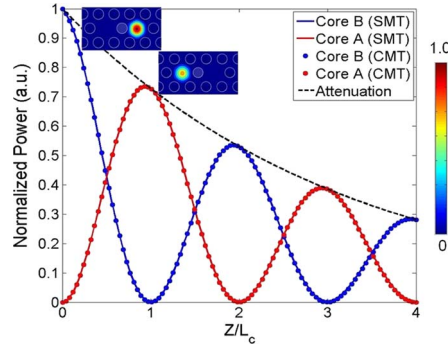
Fig. 6. Directional power transfer between the fiber cores of a DC-PCF filled with a metal wire. The black dashed line is the attenuation envelope due to the metal absorption loss at $\lambda = 1550$ nm. (Insets) Longitudinal Poynting vector plots of the new structure at $z/L_c = 0$ and $z/L_c = 1$.

significantly increases the $|\text{Re}(n_{eff}^e) - \text{Re}(n_{eff}^o)|$ value as compared with that of the conventional unfilled DC-PCF structure. Hence, the coupling length of a DC-PCF filled with a metal wire (blue curve) is more than one order of magnitude smaller than that of its counterpart (red curve), and this reduction can be maintained over a wide wavelength range. This has the potential application in miniaturized system integrations, which require a short coupling length to reduce the system size. The dip of the blue curve (inset) indicates the location of λ_r, where the coupling is the strongest, and the value of $|\text{Re}(n_{eff}^e) - \text{Re}(n_{eff}^o)|$ is the largest. In addition, L_c decreases monotonically with the wavelength and obeys a power type of relationship [17]. It is noted that L_c can also be obtained from the CMT point of view by setting $m = 0$ in (9). The CMT results are shown as blue dots in Fig. 5(a), which agree well with the SMT results. Fig. 5(b) is the L_c/L_0 ratio. L_0 is the propagation length, defined as the fiber length at which the power level in the core drops to 1/e of its original launching value. For an efficient coupler design, a ratio smaller than 1 is desirable as it means that significant amount of power can be transferred from the launching core to the other. It is shown that in our structure, this is satisfied after λ_r.

$$L_c = \frac{\pi}{|\beta_e - \beta_o|} = \frac{\lambda}{2 \times |n_{eff}^e - n_{eff}^o|} \qquad (10)$$

Fig. 6 shows a direct view of the periodic power transfer process between core A and core B as a function of the fiber length at the telecommunication window $\lambda = 1550$ nm calculated from both SMT and CMT equations. At every interval of L_c, the power transferred from one core to the other reaches the maximum, but the overall is reduced by an attenuation envelope of $\alpha = 4.77 \times 10^{-3}$ dB/μm due to the metal absorption loss. However, this may be improved by adding gain medium for the loss compensation [18], optimizing the fiber microstructure parameters or reducing the metal wire size. In any case, the loss value in our new structure is low, and as shown in the insets of the Poynting vector plots, still as high as 73.4% of the power can be transferred from the initial launching core B to core A after one L_c without any loss compensation and optimization. 73.4% is the CE, defined as the maximum percentage of power that can be coupled from the launching core to the other.

Other coupler performance indicators such as the insertion loss (IL) and the extinction ratio (ER) were also studied. IL can be approximated by the confinement loss of the coupler at L_c in our structure. ER is the ratio of the maximum output power at core A to the minimum output power at core B. At $\lambda = 1550$ nm, for our new structure, IL is 1.39 dB, and the ER value is 29.5 dB.

4.2. Optimization of Microstructure Parameters

The performance can be further improved by an optimized design of fiber microstructure parameters. Fig. 7 shows a variation of the four performance indicators with respect to λ for different
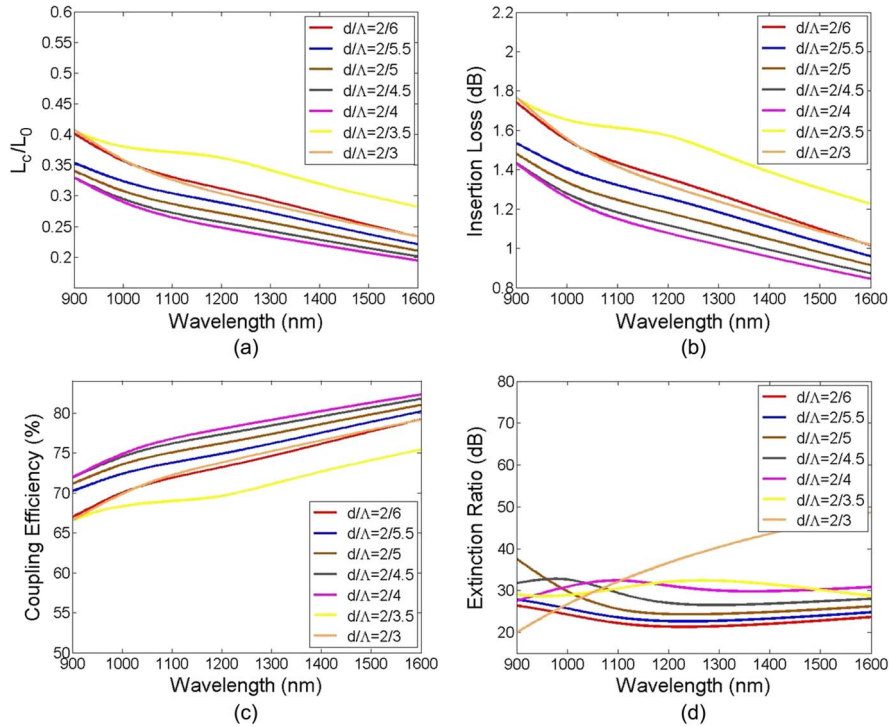
Fig. 7. Performance indicator comparison of different d/Λ ratios of a DC-PCF structure with a metal wire [Color online].

TABLE 1

Performance indicator comparison of different d/Λ ratios at a fixed wavelength $\lambda = 1550$ nm

	$d/\Lambda = 2/6$	$d/\Lambda = 2/5.5$	$d/\Lambda = 2/5$	$d/\Lambda = 2/4.5$	$d/\Lambda = 2/4$	$d/\Lambda = 2/3.5$	$d/\Lambda = 2/3$
L_c/L_0	0.24	0.23	0.22	0.21	0.20	0.29	0.24
IL (dB)	1.05	0.99	0.95	0.90	0.87	1.26	1.05
CE (%)	78.45	79.55	80.44	81.25	81.82	74.75	78.52
ER (dB)	23.22	24.38	25.83	27.70	30.54	28.13	47.39

d/Λ ratios of a DC-PCF microstructure. By varying d/Λ ratios, we have changed the SP modes and fiber core-guided modes coupling condition. Generally, the coupler performance improves (low L_c/L_0 and IL values, high CE and ER values) as d/Λ decreases; similar trends have also been reported in [13] and [19]. However, we found that further decreasing the d/Λ value would degrade the coupler performance, e.g., $d/\Lambda = 2/3.5$ and $d/\Lambda = 2/3$ compared with $d/\Lambda = 2/4$. Table 1 shows a summary of the performance indicators for different d/Λ ratios at a fixed wavelength $\lambda = 1550$ nm. The optimum value is $d/\Lambda = 2/4$ for our new structure with the lowest IL = 0.87 dB and the highest CE = 81.82%, ER = 30.54 dB comparable to other coupling devices with plasmonics effect in the literature, e.g., [8].

4.3. Optimization of Metal Inclusion Configurations

Extended structure optimization is also carried out by considering the effect of plasmonics on the coupling mechanism for different metal inclusion configurations, such as different coating positions and thickness values in the DC-PCF structure. We investigated the structures in Fig. 8, i.e., metal layer inclusion (innermost layer of air holes coated, $t_{Ag} = 40$ nm), metal tube inclusion (the center air hole coated, $t_{Ag} = 40$ nm), metal hole inclusion (the center air hole coated, $t_{Ag} = 500$ nm), and
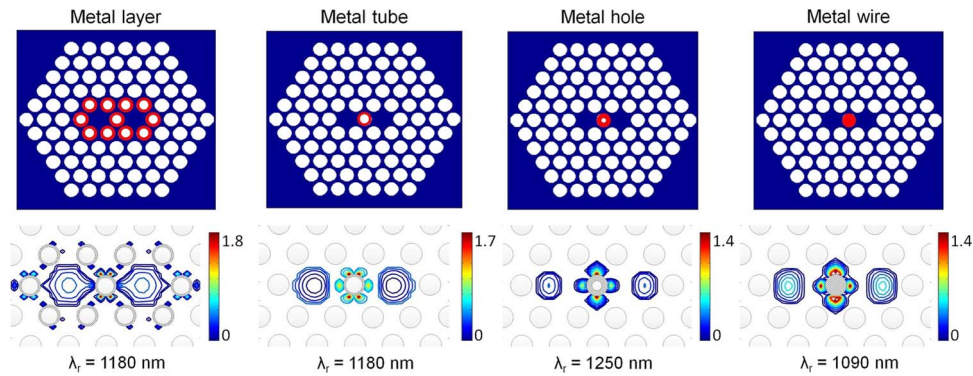
Fig. 8. Structure plots (upper) and longitudinal Poynting vector plots of modes at resonance wavelength (lower) of four different metal inclusion configurations.

TABLE 2
Performance indicator comparison of the four metal inclusion configurations at $\lambda = 1550$ nm

	Metal layer	Metal tube	Metal hole	Metal wire
L_c/L_0	2.07	0.84	0.33	0.32
IL (dB)	8.97	3.66	1.45	1.39
CE (%)	13.02	46.92	71.70	72.57
ER (dB)	15.69	11.43	36.76	25.99

metal wire inclusion (the center air hole fully coated, $t_{Ag} = 1000$ nm). These configurations were chosen because most of the energy will be confined within the core; it is likely that only the metal coating in the innermost layer of air holes closest to the core region will interact with the core-guided modes and exhibit the plasmonics phenomenon. Below the structure plots are the longitudinal Poynting vector plots of their core-guided modes at the respective resonance wavelength.

All performance indicators (L_c, IL, CE, and ER) of these four configurations are compared and shown below in Table 2 at $\lambda = 1550$ nm. We obtained these indicator values following the same analysis flow, as previously presented in Section 4.1. From the figure, we can draw the conclusion that the metal wire design outperforms the rest. For the first three configurations, their confinement loss is larger than that of the metal wire configuration. The reason is that for the metal layer configuration, the plasmonics effect can be regarded as a summation of all the SP modes contributed by each isolated metal-coated air hole [5]. However, mainly the center metal-coated hole contributes to the power transfer between the two cores; others will only scatter the core energy and, hence, increase the loss as evidenced by the Poynting vector plot. For the metal tube configuration, plasmon hybridization from the inner and outer metal–dielectric interface may happen and lead to strong metal absorption for both the even and odd supermodes, which significantly increases the confinement loss and, hence, lower the overall CE [20]. From metal tube configuration to metal hole and as the metal thickness continues to increase, the difference of the coupler performance indicators becomes less significant and tends to converge after the resonance wavelength. However, they are not the same because of the different coupling conditions of the fiber core-guided supermode and SP mode, for example, $\lambda_r = 1250$ nm for the metal hole inclusion configuration and $\lambda_r = 1090$ nm for the metal wire inclusion configuration. Overall, among the four metal inclusion configurations, the metal wire configuration is optimized for the full use of the plasmonics effect to achieve the best performance in terms of a fiber coupler design. In addition, metal wires are easier to realize in fabrication than coating metal films in the interior surface of micro-size holes in a PCF, which requires strict control of the coating uniformity and thickness as they will greatly affect the SP modes and fiber core-guided modes coupling condition. However, the control mechanism is still a challenge [21].

5. Conclusion

We have proposed a new DC-PCF structure filled with a metal wire in the center air hole. The resonant coupling between the SP modes and the fiber core-guided modes has been studied systematically using SMT and CMT with excellent agreement. The analysis shows that the new structure enhances the CE by a more than one-order-of-magnitude reduction in coupling length, which is potentially useful for miniaturized complex communication devices such as photonic integrated devices, wavelength multiplexing systems, and switches. As an example, we present salient features of our new structure as a fiber-based coupler device. Its performance optimization is discussed in terms of fiber microstructure parameter variation and different metal inclusion configurations. The new structure is compact in size and easy to fabricate. The experimental demonstration is currently being carried out in our laboratory.

References

[1] M. Skorobogatiy, K. Saitoh, and M. Koshiba, "Transverse light guides in microstructured optical fibers," *Opt. Lett.*, vol. 31, no. 3, pp. 314–316, Feb. 2006.

[2] K. Saitoh, Y. Sato, and M. Koshiba, "Coupling characteristics of dual-core photonic crystal fiber couplers," *Opt. Exp.*, vol. 11, no. 24, pp. 3188–3195, Dec. 2003.

[3] X. Yu, M. A. van Eijkelenborg, and P. Shum, "Determination of the wavelength dependence of the coupling effect in twin-core microstructured polymer optical fibers," *Opt. Eng.*, vol. 46, no. 7, pp. 075002-1–075002-5, Jul. 2007.

[4] K. S. Chiang, Y. T. Chow, D. J. Richardson, D. Taverner, L. Dong, L. Reekie, and K. M. Lo, "Experimental demonstration of intermodal dispersion in a two-core optical fibre," *Opt. Commun.*, vol. 143, no. 4–6, pp. 189–192, 1997.

[5] J. Hou, D. Bird, A. George, S. Maier, B. Kuhlmey, and J. C. Knight, "Metallic mode confinement in microstructured fibres," *Opt. Exp.*, vol. 16, no. 9, pp. 5983–5990, Apr. 2008.

[6] A. Nagasaki, K. Saitoh, and M. Koshiba, "Polarization characteristics of photonic crystal fibers selectively filled with metal wires into cladding air holes," *Opt. Exp.*, vol. 19, no. 4, pp. 3799–3808, Feb. 2011.

[7] H. K. Tyagi, H. W. Lee, P. Uebel, M. A. Schmidt, N. Joly, M. Scharrer, and P. St. J. Russell, "Plasmon resonances on gold nanowires directly drawn in a step-index fiber," *Opt. Lett.*, vol. 35, no. 15, pp. 2573–2575, Aug. 2010.

[8] Q. Li, Y. Song, G. Zhou, Y. Su, and M. Qiu, "Asymmetric plasmonic-dielectric coupler with short coupling length, high extinction ratio, and low insertion loss," *Opt. Lett.*, vol. 35, no. 19, pp. 3153–3155, Oct. 2010.

[9] H. W. Lee, M. A. Schmidt, R. F. Russell, N. Y. Joly, H. K. Tyagi, P. Uebel, and P. S. Russell, "Pressure-assisted melt-filling and optical characterization of Au nano-wires in microstructured fibers," *Opt. Exp.*, vol. 19, no. 13, pp. 12180–12189, Jun. 2011.

[10] Y. Wang, C. R. Liao, and D. N. Wang, "Femtosecond laser-assisted selective infiltration of microstructured optical fibers," *Opt. Exp.*, vol. 18, no. 17, pp. 18056–18060, Aug. 2010.

[11] R. K. Verma and B. D. Gupta, "Theoretical modelling of a bi-dimensional U-shaped surface plasmon resonance based fibre optic sensor for sensitivity enhancement," *J. Phys. D, Appl. Phys.*, vol. 41, no. 9, pp. 095106-1–095106-6, May 2008.

[12] A. K. Sharma and B. D. Rajan, "Influence of dopants on the performance of a fiber optic surface plasmon resonance sensor," *Opt. Commun.*, vol. 274, no. 2, pp. 320–326, Jun. 2007.

[13] G. Ren, S. Lou, F. Yan, and S. Jian, "Mode interference in dual-core photonic crystal fibers," in *Proc. SPIE*, Beijing, China, 2005, pp. 942–950.

[14] X. Yang, Y. Liu, R. F. Oulton, X. Yin, and X. Zhang, "Optical forces in hybrid plasmonic waveguides," *Nano Lett.*, vol. 11, no. 2, pp. 321–328, Sep. 2, 2011.

[15] K. Okamoto, *Fundamentals of Optical Waveguides,* 2nd ed.   New York: Elsevier, 2006.

[16] P. D. McIntyre and A. W. Snyder, "Power transfer between optical fibers," *J. Opt. Soc. Amer.*, vol. 63, no. 12, pp. 1518–1527, Dec. 1973.

[17] W. E. P. Padden, M. A. van Eijkelenborg, A. Argyros, and N. A. Issa, "Coupling in a twin-core microstructured polymer optical fiber," *Appl. Phys. Lett.*, vol. 84, no. 10, pp. 1689–1691, Mar. 2004.

[18] I. De Leon and P. Berini, "Amplification of long-range surface plasmons by a dipolar gain medium," *Nature Photon.*, vol. 4, pp. 382–387, 2010.

[19] X. Yu, M. Liu, Y. Chung, M. Yan, and P. Shum, "Coupling coefficient of two-core microstructured optical fiber," *Opt. Commun.*, vol. 260, no. 1, pp. 164–169, Apr. 2006.

[20] J. Zhu, "Refractive index dependent local electric field enhancement in cylindrical gold nanohole," *J. Nanoparticle Res.*, vol. 13, no. 1, pp. 87–95, 2011.

[21] J. Boehm, A. François, H. Ebendorff-Heidepriem, and T. M. Monro, "Chemical deposition of silver for the fabrication of surface plasmon microstructured optical fibre sensors," *Plasmonics*, vol. 6, no. 1, pp. 133–136, 2011.